PAPER

Check for updates

Zr- and Ce-doped Li₆Y(BO₃)₃ electrolyte for all-solid-state lithium-ion battery†

Toyoki Okumura, [iD] *[a] Yoshitaka Shiba,[b] Noriko Sakamoto,[b] Takeshi Kobayashi,[b] Saori Hashimoto,[b] Kentaro Doguchi,[b] Harunobu Ogaki,[b] Tomonari Takeuchi [iD] [a] and Hironori Kobayashi[a]

The ionic conductivity of Li₆Y(BO₃)₃ (LYBO) was enhanced by the substitution of tetravalent ions (Zr⁴⁺ and Ce⁴⁺) for Y³⁺ sites through the formation of vacancies at the Li sites, an increase in compact densification, and an increase in the Li⁺-ion conduction pathways in the LYBO phase. As a result, the ionic conductivity of Li₅.₈₇₅Y₀.₈₇₅Zr₀.₁Ce₀.₀₂₅(BO₃)₃ (ZC-LYBO) reached 1.7×10^{-5} S cm⁻¹ at 27 °C, which was about 5 orders of magnitude higher than that of undoped Li₆Y(BO₃)₃. ZC-LYBO possessed a large electrochemical window and was thermally stable after cosintering with a LiNi₁/₃Mn₁/₃Co₁/₃O₂ (NMC) positive electrode. These characteristics facilitated good reversible capacities in all-solid-state batteries for both NMC positive electrodes and graphite negative electrodes *via* a simple cosintering process.

Introduction

The steady evolution of new crystal systems with high ionic conductivities has recently heightened expectations for the realisation of all-solid-state batteries (ASSBs).[1] Indeed, the successful demonstration of a high-rate-capacity ASSB has been reported with 10^{-2} S cm⁻¹-class Li₁₀GeP₂S₁₂ (LGPS)-type sulfide-based electrolytes.[2] In the case of oxides, the reported conductivities of $\approx 10^{-3}$ S cm⁻¹ in current oxide-based crystal systems (perovskites,[3] NASICON types,[4] and garnets[5]) have encouraged the realisation of oxide-based ASSBs because they are approaching the conductivities of non-aqueous liquid electrolytes ($\approx 10^{-2}$ S cm⁻¹). Oxide-based ASSBs are expected to be applied as on-board power sources for next-generation wireless Internet-of-Things devices because of their long-life performance and thermal stability. However, the discovery of better ion-conductive oxides is not always related to the enhancement of the performance of oxide-based ASSBs. This corresponds to another issue, that is, the difficulty of impurity-free interface formation between the active materials and oxide electrolyte during cosintering.[6–10] Therefore, oxide-based ionic conductors that are both highly conductive and thermally stable with respect to the electrode materials are required for the development of electrolytes for sintered oxide-based ASSBs.

The Li₃BO₃-related families have been considered as suitable electrolytes for fabricating good contacts at the electrode/electrolyte interface by cosintering. For example, Li₃BO₃ was used as an interfacial additive between LiCoO₂ electrode particles and a garnet-type sintered electrolyte plate, and reversible charge–discharge capacities were demonstrated for the ASSB after cosintering at 700 °C, despite the low conductivity of Li₃BO₃ ($\sigma < 10^{-7}$ S cm⁻¹ at 150 °C).[11,12] In a later report, a solid solution of Li₂CO₃ and Li₃BO₃, Li₂.₂C₀.₈B₀.₂O₃, was described as a superior candidate for assembling the ASSB because of its better conductivity of $\approx 10^{-6}$ S cm⁻¹ at 25 °C.[13,14] Two other Li₃BO₃-related electrolytes—Li₃BO₃–Li₂SO₄ amorphous materials[15] and LISICON-Li₃BO₃ amorphous materials[16]—were also attractive candidates, but the ASSBs were assembled according to their deformability due to their amorphous character rather than their thermal stability.

Among Li₃BO₃-related families, Lopez-Bermudez *et al.* proposed a solid solution of YBO₃ and Li₃BO₃, that is, Li₆Y(BO₃)₃ (LYBO), as a new crystal-type electrolyte candidate.[17] The observed ionic conductivity was low at 1.9×10^{-8} S cm⁻¹ at 50 °C because Li⁺-ion diffusion was permitted only by thermodynamic point-defect formation in the Li₆Y(BO₃)₃. However, based on DFT calculations of the defect-formation energies and Li⁺-ion diffusion barriers, they suggested the structural superiority of Li⁺-ion diffusion in the LYBO-type structure, and mentioned the possibility of conductivity enhancement by aliovalent substitution.[17]

In the present study, we prepared tetravalent ion (Zr⁴⁺ and Ce⁴⁺)-doped LYBO-type materials and confirmed an ionic conductivity enhancement to $\approx 10^{-5}$ S cm⁻¹ at 27 °C.

[a]Research Institute of Electrochemical Energy, National Institute of Advanced Industrial Science and Technology (AIST), Midorigaoka 1-8-31, Ikeda, Osaka 563-8577, Japan. E-mail: toyoki-okumura@aist.go.jp

[b]Development Division, Canon Optron Inc., Kanakubo1744-1, Yuki, Ibaraki 307-0015, Japan

Furthermore, the performance of oxide-based ASSBs was successfully demonstrated with the Zr- and Ce-doped $Li_{5.875}$-$Y_{0.875}Zr_{0.1}Ce_{0.025}(BO_3)_3$ (ZC-LYBO) electrolyte because of its thermal stability to layered rock-salt positive electrodes, such as the $LiNi_{1/3}Mn_{1/3}Co_{1/3}O_2$ (NMC) positive electrode, and its large electrochemical window.

Experimental

Tetravalent ion-containing LYBO samples with various molar ratios, $Li_{6-x-y}Y_{1-x-y}Zr_xCe_y(BO_3)_3$, were prepared using Li_3BO_3 (99.9% purity, Toshima Manufacturing Co., Japan), H_3BO_3 (99.5% purity, Kanto Chemical Co., Japan), Y_2O_3 (99.9% purity, Shin-Etsu Chemical Co., Japan), ZrO_2 (99.9% purity, Nippon Denko Co., Japan), and CeO_2 (99.9% purity, Shin-Etsu) as starting materials. An appropriate amount of each compound was weighed to obtain the desired molar ratio, and the mixture was ground using a mechanical milling technique (Pulverisette7, Fritsch). The mixture was pelletized and heated at 650 °C for 12 h. The reacted product was ground and sintered by spark-plasma sintering (SPS) at 600–700 °C for 10 min under a pressure of 30 MPa, to produce the tetravalent ion-containing LYBO compacts.

The structural changes and purities of the samples were evaluated using synchrotron X-ray diffraction (SXRD) analysis (0.5 Å) performed at BL19B2, SPring-8, Sayo, Japan (2019B1881). Rietveld crystal structure refinement of the obtained SXRD patterns was performed using the RIETAN-FP software program,[18] where a modified split pseudo-Voigt function[19] was selected for fitting to best represent the profile parameters of the samples. To estimate the Li^+-ion diffusion pathways in the structure, the refined structural parameters were used as the input file for bond valence site energy (BVSE) calculations, which were performed using SoftBV software.[20,21] The structural images and maps were drawn using the VESTA software program.[22]

For ion conductivity measurements, both sides of the tetravalent ion-containing LYBO compacts were polished and coated with gold (via sputtering) as blocking electrodes. The AC impedance profile was collected with a frequency response analyser (Solartron, 1296) over a frequency range of 0.1 Hz to 1 MHz at 27 °C.

To measure the charge–discharge performance of the ASSB, a composite electrode powder consisting of 50 wt% active material and 50 wt% ZC-LYBO electrolyte was first prepared by mixing in an agate mortar. The active material was either $LiNi_{1/3}Mn_{1/3}Co_{1/3}O_2$ (NMC, Toda Kogyo Corp.) or graphite (JFE Chemical Corp.). The composite electrode powder (10 mg) and a Au plate as a current collector were placed on a ZC-LYBO-electrolyte separator of 30 mg in a 10 mm-diameter carbon die, which was heated at 550 °C with an electric current under a pressure of 30 MPa in the SPS process. Lithium foil was used as the counter electrode. A polyethylene oxide (PEO)-based polymer electrolyte film (Osaka Soda, LiTFSA/EO = 0.06) was placed between the lithium foil and the electrolyte side of the composite electrode/electrolyte pellet to reduce the interfacial resistance via adhesion.[13]

To confirm the reactivity of the composite electrode after cosintering, laboratory XRD patterns were collected on a diffractometer using Cu Kα radiation (Miniflex600, Rigaku). All XRD analyses were performed in the Bragg–Brentano geometry mode. The microstructure of the composite electrode was observed using field-emission scanning electron microscopy (FE-SEM; JEOL, JSM-5500LV).

To evaluate the electrochemical stability of the ZC-LYBO electrolyte, a metal substrate (Au or Cu) was placed on a ZC-LYBO electrolyte (100 mg) in a 10 mm-diameter carbon die, which was heated at 550 °C with an electric current under a pressure of 30 MPa in the SPS process. Lithium foil and a PEO-based polymer electrolyte film were used as the counter electrode and interfacial connector, respectively.

Results and discussion

Structural changes and purities of tetravalent ion-doped LYBO

Fig. 1 shows the SXRD patterns of the Zr^{4+} ion-containing LYBO samples, $Li_{6-x}Y_{1-x}Zr_x(BO_3)_3$ ($0 \leq x \leq 0.6$). The $I(1\ 1\ -2)$ diffraction peak is clearly shifted to a higher angle with an increasing amount of Zr^{4+} until $x \approx 0.1$ in $Li_{6-x}Y_{1-x}Zr_x(BO_3)_3$ because of the difference in ionic radii: 1.019 Å for Y^{3+} and 0.84 Å for Zr^{4+} in dodecahedral coordination.[23] In addition, the $I(1\ 1\ -2)$ diffraction peak is broadened with an increasing amount of Zr^{4+} ions, which corresponds to the lattice distortion of the LYBO-type structure in addition to the aforementioned mismatch of ionic radii, which will be discussed later. Furthermore, the ZrO_2 impurity phase begins to appear from $x \approx 0.1$.
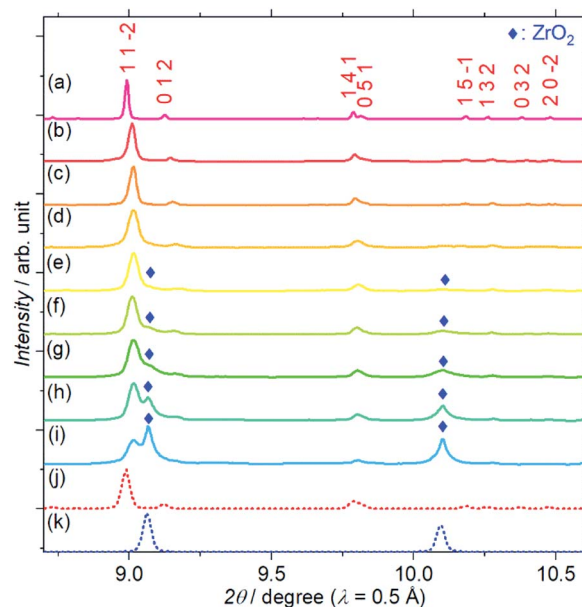

Fig. 1 Synchrotron X-ray diffraction patterns of $Li_{6-x}Y_{1-x}Zr_x(BO_3)_3$, where x = (a) 0, (b) 0.025, (c) 0.05, (d) 0.075, (e) 0.1, (f) 0.2, (g) 0.3, (h) 0.4, (i) 0.6. Simulated patterns for (j) $Li_6Y(BO_3)_3$ (red dashed line) and (k) ZrO_2 (blue dashed line) are also shown. The patterns associated with the ZrO_2 impurity phase are represented by blue diamonds.

Rietveld refinements of the SXRD patterns were performed to clarify the structural changes caused by the Zr^{4+} ions. The refined patterns for typical samples and the estimated parameters for all the samples are summarised in Fig. S2(a–c), and Table S1,† respectively. Fig. 2(a) shows the changes in the cell volume and full-width-at-half-maximum (FWHM) parameter U for the LYBO-type phases estimated from the refinements. Herein, U is one of the simulated components for representing the FWHMs of the total diffraction patterns based on the Caglioti formula[24] under Rietveld refinement.

$$FWHM^2 = U \tan^2 \theta_{Bragg} + V \tan \theta_{Bragg} + W$$

where parameters V and W mainly depend on the diffractometer characteristics, which were estimated from the refinements of a CeO_2 reference in advance, and θ_{Bragg} is the diffraction peak angle.

Thus, U represents the FWHM corresponding to the structural distortion in a sample. It should be noted that the structural distortion is difficult to discuss quantitatively in this study because a modified split pseudo-Voigt function[19] was used to refine the profiles. Despite the difficulties in this case, the definite change in U due to the Zr^{4+} ion is strongly related to the structural distortion until $x \approx 0.1$ in $Li_{6-x}Y_{1-x}Zr_x(BO_3)_3$, which is due to the substitution of smaller Zr^{4+} ions at the Y^{3+} sites. The shrinkage of the cell volume until $x \approx 0.1$ is also proof of Zr^{4+}-ion doping. When $x > 0.1$, these changes are suppressed because of the limits of Zr^{4+}-ion doping into the LYBO-type structure; thereafter, the ZrO_2 impurity (and Li–B–O impurities, mainly $Li_6B_4O_9$) is observed. Moreover, the lattice parameter b and area of the ac plane are shown separately in Fig. 2(b). The LYBO-type structure has a layered structure that is constructed by the stacking of the $Li_2Y(BO_3)_3$ layer and the Li layer along the b-axis, as shown in Fig. 3(a). The shrinkage of the YO_8 dodecahedra upon doping with smaller Zr^{4+} ions until $x \approx 0.1$ directly reduces the area of the ac plane. On the other hand, the lattice parameter b is expanded until $x \approx 0.1$ because of the decrease in Coulomb repulsion force at the Li layer due to the lack of Li^+ ions under the doping of Zr^{4+} ions into $Li_{6-x}Y_{1-x}Zr_x(BO_3)_3$. This tendency is similar to the change in the lattice parameter c during the electrochemical de-lithiation of layered rock-salt $Li_{1-x}CoO_2$.[25] Therefore, Li^+ ions are likely to be removed from the Li layer rather than from the $Li_2Y(/Zr)(BO_3)_3$ layer by doping Zr^{4+} ions into $Li_{6-x}Y_{1-x}Zr_x(BO_3)_3$, which is supported by previous DFT calculation results in which the Li defect energies at the Li layer are lower than those at the $Li_2Y(BO_3)_3$ layer in $Li_6Y(BO_3)_3$.[17]

Li-ion conductive pathways

The Li^+-ion diffusion pathways in the LYBO-type structure were examined from bond-valence site energy (BVSE) maps; the ab and ac planes are shown in Fig. 3(b–d) and S3(b–d),† respectively. The BVSE maps present the theoretical mobile Li^+-ion pathways as clouds with low bond valence site energies. Although the mobile Li^+ ions form a 2D diffusion pathway network at the Li layer on the ac plane [Fig. S3(b)†], it is difficult for Li^+ ions to diffuse along the b axis via Li3 or Li5 sites in undoped $Li_6Y(BO_3)_3$, as shown by the red dashed boxes in Fig. 3(b). This was previously suggested from DFT calculations.[17] As shown in Fig. 3(c, d), the expansion of the diffusion pathways along the b-axis could be induced by doping Zr^{4+} ions into $Li_{6-x}Y_{1-x}Zr_x(BO_3)_3$, which indicates that the structural
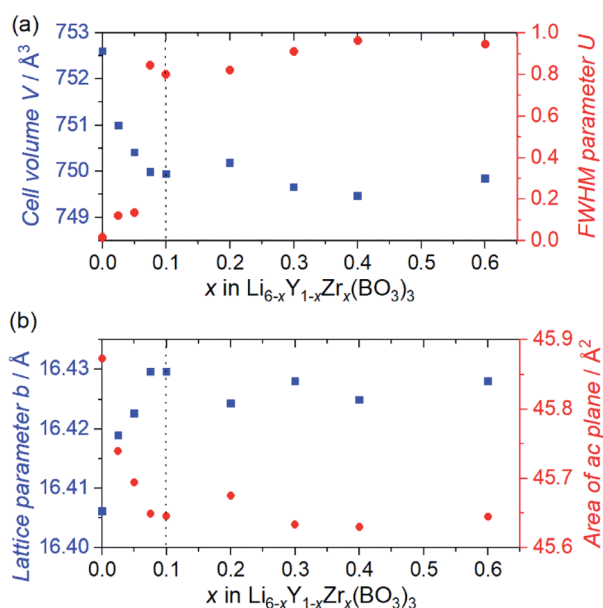

Fig. 2 (a) Cell volumes V (blue squares) and FWHM parameters U (red circles), and (b) lattice parameters b (blue squares) and areas of ac plane (red circles) for Zr-doped $Li_{6-x}Y_{1-x}Zr_x(BO_3)_3$, as estimated by Rietveld refinements of the synchrotron X-ray diffraction patterns.
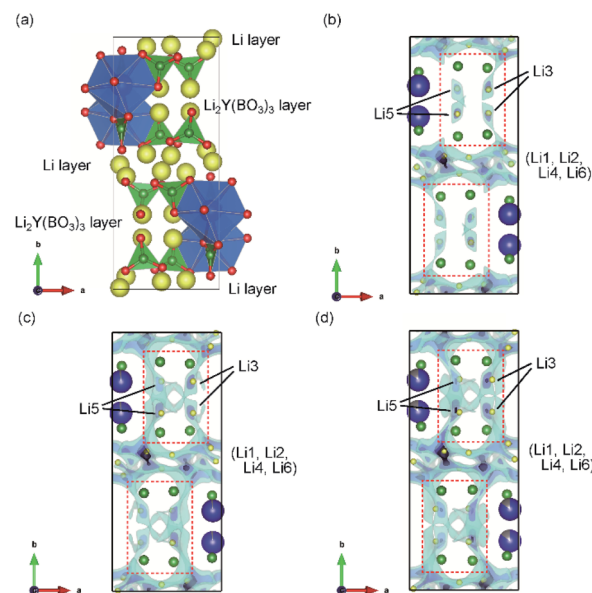

Fig. 3 (a) Schematic representation of LYBO-type structure. Blue dodecahedra represent $Y(/Zr)O_8$, green triangles represent BO_3, and yellow balls indicate Li ions. 3D BVSE maps of the ab plane for (b) undoped $Li_6Y(BO_3)_3$, (c) Zr-doped $Li_{5.975}Y_{0.975}Zr_{0.025}(BO_3)_3$, and (d) Zr-doped $Li_{5.9}Y_{0.9}Zr_{0.1}(BO_3)_3$. Translucent clouds of light blue represent the regions of low bond valence site energy for Li^+ ions.

distortion in the $Li_2Y(/Zr)(BO_3)_3$ layer contributed to expanding the diffusion pathways. The 2D diffusion pathways in the Li layer also become thin, as can be confirmed from Fig. S3(c, d).† These results indicate that Li^+ ions are more easily diffused by the structural distortion associated with doping Zr^{4+} ions into $Li_{6-x}Y_{1-x}Zr_x(BO_3)_3$. The activation energies for the 2D and 3D pathways estimated from BVSE decrease from 0.57 and 0.69 eV to 0.49 and 0.59 eV, respectively, even by doping with only $x = 0.025$ Zr^{4+} ions into $Li_{6-x}Y_{1-x}Zr_x(BO_3)_3$.

Ionic conductivities

Fig. 4 shows the ionic conductivity dependence when Zr^{4+} ions are incorporated into $Li_{6-x}Y_{1-x}Zr_x(BO_3)_3$ ($0 \leq x \leq 0.1$). The observed conductivity at 27 °C is drastically enhanced from 5.6×10^{-11} to 5.8×10^{-6} S cm^{-1} by doping with $x = 0.025$ Zr^{4+} ions into $Li_{6-x}Y_{1-x}Zr_x(BO_3)_3$. Li^+-ion diffusion in Li-ion fully occupied $Li_6Y(BO_3)_3$ occurs only through the formation of a few thermodynamic point defects. In contrast, the substitution of tetravalent Zr^{4+} ions in the Y^{3+} sites results in the intentional formation of vacancies at Li sites in the structure, which contributes to the conductivity enhancement. Additionally, the observed conductivities are sensitive to the relative densities of the $Li_{6-x}Y_{1-x}Zr_x(BO_3)_3$ compacts, which are summarised in Table S2.† For example, the observed conductivity in a low-density $Li_{3.5}Ge_{0.75}S_{0.25}O_4$ compact (79%) was over a hundred times lower than a high density compact (~90%).[26] Therefore, the increase in relative density upon doping with Zr^{4+} ions, from 77% ($x = 0$) to ~90% ($x > 0$), also contributes to the ionic conductivity enhancement. Moreover, the expansion of 3D diffusion pathways by Zr^{4+} doping, as estimated by the Rietveld analyses, would also affect the enhancement. To confirm this effect, the structure and conductivity of Ce-doped $Li_{5.975}Y_{0.975}Ce_{0.025}(BO_3)_3$ were also

examined. The ionic radius for the Ce^{4+} ion dopant in dodecahedral coordination is 0.97 Å, which is more comparable to that for the Y^{3+} ion (1.019 Å) than the Zr^{4+} ion dopant (0.84 Å).[23] Therefore, the lattice distortion by doping the tetravalent ion is supressed; the lattice distortion in Ce-doped $Li_{5.975}Y_{0.975}Ce_{0.025}(BO_3)_3$ ($U = 0.02354$ deg^2) is closer to that in undoped $Li_6Y(BO_3)_3$ ($U = 0.01488$ deg^2) than that in Zr-doped $Li_{5.975}Y_{0.975}Zr_{0.025}(BO_3)_3$ ($U = 0.119$ deg^2), as can be confirmed in Table S1.† Considering the conductivities shown in Table S3,† that of the LYBO-type structure is drastically enhanced by 0.025 Ce^{4+} doping ($Li_{5.975}Y_{0.975}Ce_{0.025}(BO_3)_3$; $\sigma = 6.9 \times 10^{-7}$ S cm^{-1} at 27 °C), which is due to the formation of vacancies at Li sites in the structure and the increase in compact densification, as discussed above. However, the conductivity of the Ce^{4+}-ion doped sample is over ten times lower than that of the Zr^{4+}-ion doped one. This difference indicates that the structural distortion associated with the doping of the larger Zr^{4+} ions certainly affects the enhancement of the conductivity. The differences in the Li^+-ion diffusion pathways estimated from the BVSE maps also support the aforementioned results: for the less-structurally-distorted Ce^{4+}-ion doped sample (Fig. S4(a, b)†), the diffusion pathway along the b-axis in the BVSE map is nearly unchanged. Therefore, Zr^{4+}-ion doping exerts three types of effects that enhance the conductivity of the LYBO-type structure: (1) the formation of vacancies at Li sites, (2) an increase in compact densification, and (3) an increase in the Li^+-ion conduction pathways in the LYBO phase associated with structural distortion. The highest conductivity in Zr^{4+}-ion-doped $Li_{6-x}Y_{1-x}Zr_x(BO_3)_3$ at 27 °C is 1.4×10^{-5} S cm^{-1} at $x = 0.10$. However, Zr^{4+}-ion doping achieves a limit at $x \approx 0.1$ in $Li_{6-x}Y_{1-x}Zr_x(BO_3)_3$, which would be due to the large mismatch of ionic radii. Therefore, the conductivity decreases for $x > 0.1$ (Table S3†), with increases in the amounts of ZrO_2 and Li–B–O impurities.

The conductivity of Zr,Ce-doped $Li_{5.875}Y_{0.875}Zr_{0.1}Ce_{0.025}Zr_{0.1}(BO_3)_3$ (ZC-LYBO) was also measured, and the obtained value of 1.7×10^{-5} S cm^{-1} at 27 °C is the highest conductivity of LYBO-type oxides to date. The structural information estimated from Rietveld analysis, Li^+-ion diffusion pathways estimated from BVSE maps, and relative densities of the compacts are summarised in Table S1, Fig. S3(d), and Table S2.† Compared with Zr-doped $Li_{5.9}Y_{0.9}Zr_{0.1}(BO_3)_3$, a slight enhancement in conductivity is confirmed, but the reason is difficult to determine in the present study. The conductivity measurement results indicate the possibility of further enhancement by other aliovalent substitutions. Moreover, the control of structural distortion is one of the keys for enhancing the conductivity of the LYBO-type structure. It should be noted that the activation energies estimated from Arrhenius plots (Fig. S5†) were 0.43 eV for both Zr-doped $Li_{5.9}Y_{0.9}Zr_{0.1}(BO_3)_3$ and Zr,Ce-doped $Li_{5.875}Y_{0.875}Ce_{0.025}Zr_{0.1}(BO_3)_3$ (ZC-LYBO). Based on its high conductivity, ZC-LYBO was used as the electrolyte in subsequent ASSB studies.

Thermal stability after cosintering with layered rock-salt oxide active material

The reactivity of the layered rock-salt $LiNi_{1/3}Mn_{1/3}Co_{1/3}O_2$ (NMC) electrode and ZC-LYBO electrolyte after cosintering was
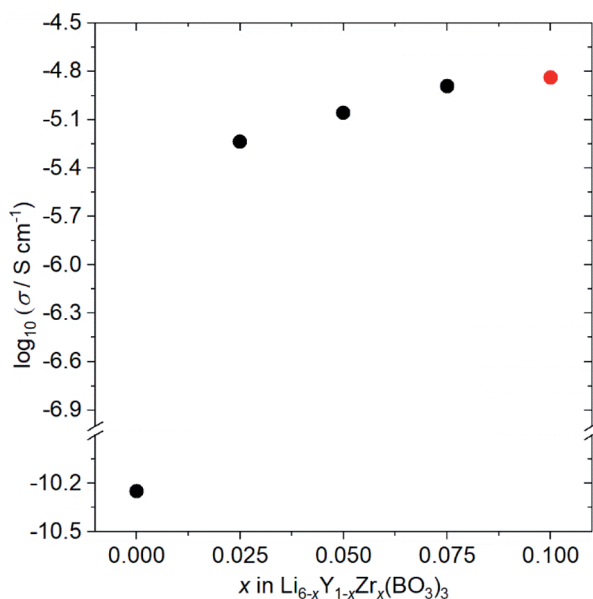

Fig. 4 Ionic conductivity dependence on the composition of $Li_{6-x}Y_{1-x}Zr_x(BO_3)_3$ ($0 \leq x \leq 0.10$) at 27 °C. $Li_{5.9}Y_{0.9}Zr_{0.1}(BO_3)_3$ ($x = 0.10$) contains small amount of ZrO_2 impurity (red circle).
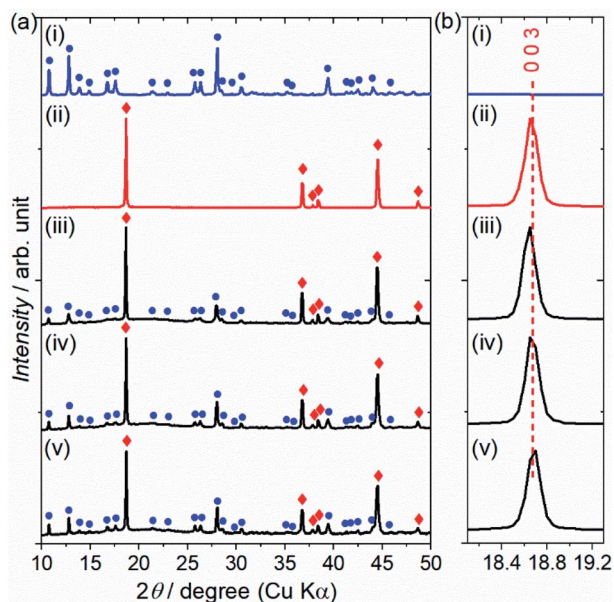
Fig. 5 (a) Laboratory XRD patterns of (i) ZC-LYBO, (ii) NMC, and the NMC−ZC-LYBO combinations after SPS at (iii) 450 °C, (iv) 550 °C, and (v) 650 °C. Typical diffraction peaks for ZC-LYBO and NMC are represented by blue circles and red diamonds, respectively. (b) The significant diffraction positions at *I*(0 0 3) for NMC.

evaluated by laboratory XRD patterns (Fig. 5(a)). None of the XRD peaks are associated with impurities, and no significant peak shifts after co-sintering are observed for either the NMC electrode or ZC-LYBO electrolyte, as shown for a typical peak in Fig. 5(b). Thus, interdiffusion between the NMC and ZC-LYBO was minimal, with no penetration of the bulk materials during cosintering. This result indicates that ZC-LYBO is thermally stable with a layered rock-salt NMC electrode.

The cross-sectional microstructure of the NMC + ZC-LYBO composite electrode after the 550 °C SPS process was also
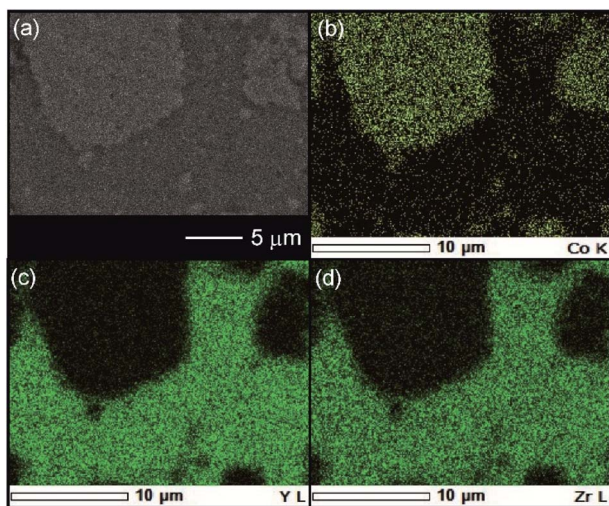
investigated. As shown in Fig. 6(a), the NMC electrode particles (light grey) are embedded in the ZC-LYBO electrolyte (dark grey). Moreover, no micropores are present near the NMC electrodes because the ZC-LYBO electrolyte was densified after SPS. No evidence of diffusion is found in the EDX mappings for Co [NMC electrode, Fig. 6(b)], Y, and Zr [ZC-LYBO electrolyte, Fig. 6(c and d)]. This indicates that the ZC-LYBO electrolyte and NMC electrode can be co-sintered without the formation of any interfacial impurities, which is one of the rare characteristics of the electrolyte and is not possible with other popular oxide-electrolyte candidates (*e.g.* perovskite-type conductors, NASI-CONs, and garnet-type conductors).

Fig. 7(a) shows the charge–discharge profiles for an ASSB (NMC + ZC-LYBO composite electrode|ZC-LYBO separator|dry polymer|Li metal) assembled *via* SPS. A reversible capacity of ~120 mA h g^{-1} is observed at 60 °C owing to the impurity-free sintered interface between the NMC and ZC-LYBO. The charge–discharge capacity retentions at various current densities are shown in Fig. 7(b). Although the capacity decreases at higher current densities, relatively stable capacity retention under cycling for each current density is observed for the ASSB. In fact, the rate performance of the ASSB using the ZC-LYBO electrolyte is lower than that using LISICON-type $Li_{3.5}Ge_{0.5}V_{0.5}O_4$ (LGVO), which has also been reported as a thermally stable electrolyte with an NMC electrode.[27] This is due to the lower conductivity of ZC-LYBO compared to $Li_{3.5}Ge_{0.5}V_{0.5}O_4$ (*i.e.* 9.6×10^{-5} S cm^{-1} at

Fig. 7 (a) Electrochemical charge−discharge profiles of an ASSB (Au|NMC + ZC-LYBO composite electrode|ZC-LYBO separator|dry polymer|Li metal) prepared *via* SPS at 550 °C over three charge−discharge cycles at a constant current of 64 μA cm^{-2} at 60 °C. (b) Charge−discharge capacity retentions of the ASSB at different current densities at 60 °C.

Fig. 6 (a) Cross-sectional SEM image at the NMC−ZC-LYBO interface after SPS at 550 °C, with the corresponding EDX elemental maps for (b) Co, (c) Y, and (d) Zr.

25 °C).[27] However, a broader acceptance of aliovalent substitutions in the less-reported LYBO-type electrolytes could lead to the development of a more highly ion-conductive LYBO family, analogous to the advances achieved with other electrolyte candidates.[1]

Electrochemical window

Fig. 8(a) shows the cyclic voltammograms (CVs) of test cells (metal substrate|ZC-LYBO electrolyte|dry polymer|Li metal) assembled by SPS. We evaluated the electrochemical stability of the ZC-LYBO electrolyte in the low-voltage range from 3.0 to −0.5 V vs. Li/Li$^+$ and in the high-voltage range from 2.0 to 5.0 V vs. Li/Li$^+$ with a Cu substrate (red) and an Au substrate (blue), respectively. The ZC-LYBO electrolyte is stable at high voltages. Au is kinetically stable within a wide electrochemical window but produces Li$_x$Au$_y$ alloys at voltages below 0.2 V vs. Li/Li$^+$ when in contact with Li metal.[28,29] Therefore, Cu was used as the substrate to evaluate the low-voltage stability.[30] Cathodic and anodic currents corresponding to Li metal deposition (Li$^+$ + e$^-$ → Li) and dissolution (Li → Li$^+$ + e$^-$), respectively, are observed at 0 V vs. Li/Li$^+$. Although the ZC-LYBO electrolyte is nearly electrochemically stable in the range from 0.0 to 5.0 V vs. Li/Li$^+$, a slight cathodic peak can be observed below ≈1.0 V vs. Li/Li$^+$.

Fig. 8 (a) Cyclic voltammograms (CVs) of test cells (metal substrate|ZC-LYBO electrolyte|dry polymer|Li metal) prepared by the 550 °C-SPS process at a scan rate of 100 μV s^{-1} at 60 °C. Cu and Au metal substrates were used for testing the cathodic and the anodic reactions, respectively. (b) Nyquist plots of the test cell using Cu substrate at 60 °C after the CV cycling and the CV profile at each cycle.
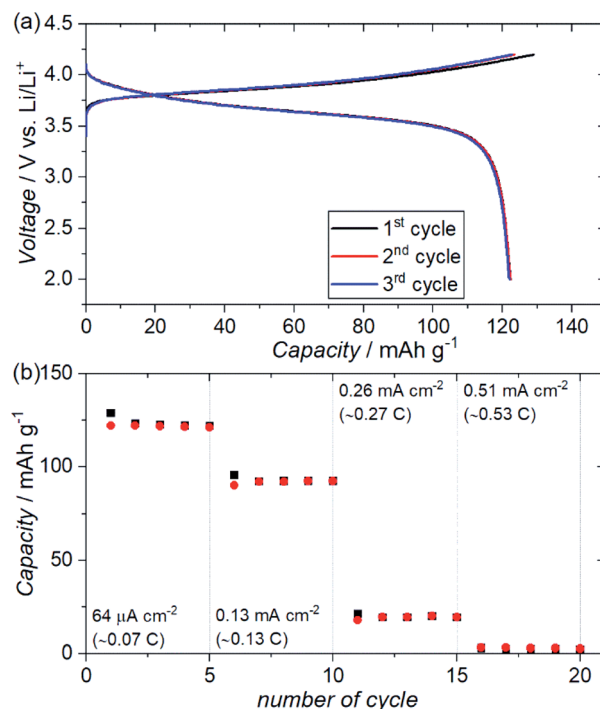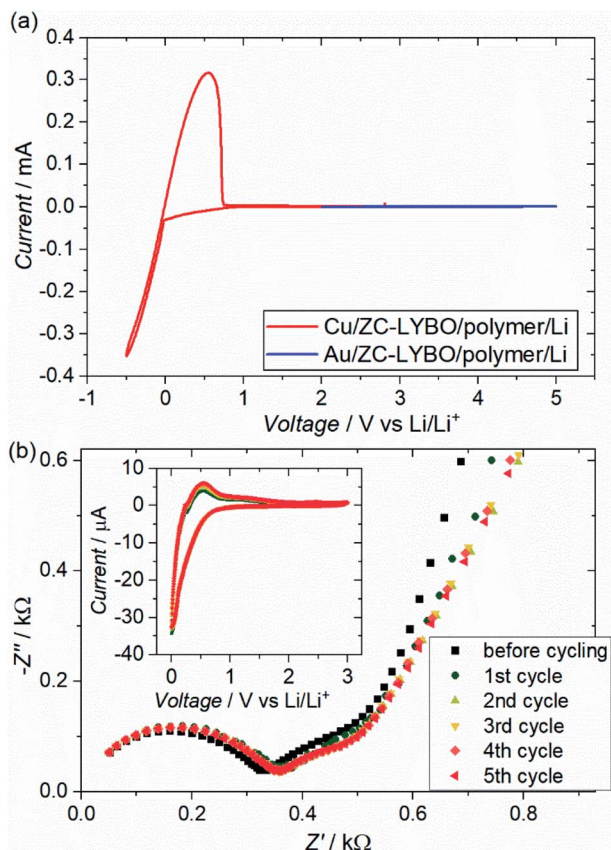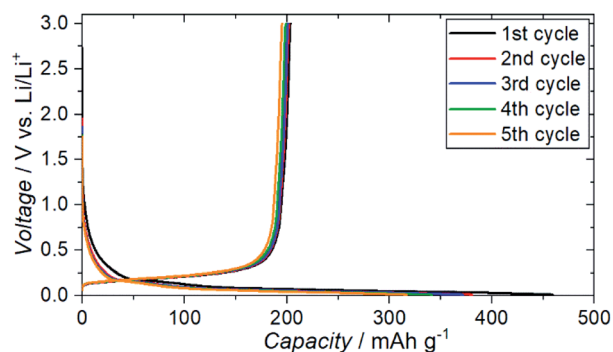

Fig. 9 Electrochemical charge–discharge profiles of Cu|graphite + ZC-LYBO composite electrode|ZC-LYBO separator|dry polymer|Li metal.

Thus, the CVs under 5 cycles in the range from 3.0 to 0.0 V vs. Li/Li$^+$ were also recorded (Fig. 8(b), insert). A slight cathodic peak continuously appears in each CV cycle and is irreversible, which would result in decomposition on the surface of the ZC-LYBO electrolyte at low voltage. Fig. 8(b) shows the conductivity change for the LYBO electrolyte after each CV cycle. Despite the continuous appearance of a cathodic peak, the Nyquist plots, including the resistance in the ZC-LYBO electrolyte, change less. Therefore, ZC-LYBO can also be used as an electrolyte with a low-voltage negative electrode.

The charge–discharge profiles for a battery (Cu|graphite negative electrode + ZC-LYBO composite electrode|ZC-LYBO separator|dry polymer|Li metal) assembled by the SPS process are shown in Fig. 9. A typical reversible Li-ion (de)intercalation reaction for a graphite negative electrode is observed, and a first discharge capacity of ∼200 mA h g^{-1} was obtained along with a large irreversible capacity for each cycle. The irreversible capacity is related to the slight anodic reaction below 1.0 V Li/Li$^+$ (Fig. 8).

Among the various oxide-type electrolytes, ZC-LYBO is rare; it is possible to assemble ASSBs by sintering with both layered lock-salt positive electrodes such as NMC and low-voltage negative electrodes such as graphite. LISICON-type Li$_{3.5}$Ge$_{0.5}$-V$_{0.5}$O$_4$ (LGVO) can also be cosintered with layered rock-salt positive electrodes but decompose at low voltage because of the presence of Ge^{4+} and V^{5+} ions.[27] In fact, other Li$_3$BO$_3$-related families such as Li$_{2.2}$C$_{0.8}$B$_{0.2}$O$_3$ (ref. 13 and 14) and LISICON-Li$_3$BO$_3$ (ref. 16) are stable at low voltage, although conductivities are limited to ≈10^{-6} S cm^{-1} at 25 °C. Therefore, the LYBO-type crystal system may be an attractive candidate for assembling ASSBs by sintering after further enhancing the conductivity via aliovalent substitution. Even the ZC-LYBO in the present study can be used as an ion-conductive ceramic binder for sintering ASSBs instead of low-ion-conductive Li$_3$BO$_3$,[12] which has been used to connect LiCoO$_2$ electrodes and high-ion-conductive garnet-type electrolytes.[11]

Conclusions

We substituted tetravalent ions (Zr^{4+} and Ce^{4+}) for the Y^{3+} sites in the Li$_6$Y(BO$_3$)$_3$ (LYBO)-type structure to enhance conductivity.

The ionic conductivities of Zr-doped $Li_{5.9}Y_{0.9}Zr_{0.1}(BO_3)_3$ and Zr,Ce-doped $Li_{5.875}Y_{0.875}Ce_{0.025}Zr_{0.1}(BO_3)_3$ (ZC-LYBO) were respectively 1.4×10^{-5} and 1.7×10^{-5} S cm^{-1} at 27 °C, which are some of highest conductivities reported for Li_3BO_3-related electrolyte candidates. The effects of Zr^{4+}-ion doping on the conductivity of the LYBO-type structure were revealed from the structural information estimated from Rietveld analysis, relative density of compacts, and Li^+-ion diffusion pathways estimated from BVSE maps, and included: (1) the formation of vacancies at Li sites, (2) the increase of compact densification, and (3) an increase in the Li^+-ion conduction pathways in the LYBO phase associated with structural distortion.

Furthermore, sintered ASSBs using ZC-LYBO as an electrolyte successfully performed with both a $LiNi_{1/3}Mn_{1/3}Co_{1/3}O_2$ (NMC) positive electrode and a graphite negative electrode. This was due to the thermal stability of the layered rock-salt oxide and the electrochemical stability of the ZC-LYBO at low voltages. The conductivity of the LYBO-type electrolyte could be further enhanced by other aliovalent substitutions for the practical use of sintered ASSBs. The control of the structural distortion associated with the dopant size, which was revealed in this study, could play an important role in this enhancement.

Conflicts of interest

There are no conflicts to declare.

Acknowledgements

References

1 F. Zheng, M. Kotobuki, S. Song, M. O. Lai and L. Lu, *J. Power Sources*, 2018, **389**, 198–213.

2 N. Kamaya, K. Homma, Y. Yamakawa, M. Hirayama, R. Kanno, M. Yoneyama, T. Kamiyama, Y. Kato, S. Hama, K. Kawamoto and A. Mitsui, *Nat. Mater.*, 2011, **10**, 682–686.

3 Y. Inaguma, C. Liquan, M. Itoh, T. Nakamura, T. Uchida, H. Ikuta and M. Wakihara, *Solid State Commun.*, 1993, **86**, 689–693.

4 G. Adachi, N. Imanaka and H. Aono, *Adv. Mater.*, 1996, **8**, 127–135.

5 V. Thangadurai, H. Kaack and W. J. F. Weppner, *J. Am. Ceram. Soc.*, 2003, **86**, 437–440.

6 G. Vardar, W. J. Bowman, Q. Lu, J. Wang, R. J. Chater, A. Aguadero, R. Seibert, J. Terry, A. Hunt, I. Waluyo, D. D. Fong, A. Jarry, E. J. Crumlin, S. L. Hellstrom, Y. Chiang and B. Yildiz, *Chem. Mater.*, 2018, **30**, 6259–6276.

7 K. Park, B. C. Yu, J. W. Jung, Y. T. Li, W. D. Zhou, H. C. Gao, S. Son and J. B. Goodenough, *Chem. Mater.*, 2016, **28**, 8051–8059.

8 L. Miara, A. Windmuller, C. L. Tsai, W. D. Richards, Q. L. Ma, S. Uhlenbruck, O. Guillon and G. Ceder, *ACS Appl. Mater. Interfaces*, 2016, **8**, 26842–26850.

9 M. Gellert, E. Dashjav, D. Gruner, Q. L. Ma and F. Tietz, *Ionics*, 2018, **24**, 1001–1006.

10 M. F. Groh, M. J. Sullivan, M. W. Gaultois, O. Pecher, K. J. Griffith and C. P. Grey, *Chem. Mater.*, 2018, **30**, 5886–5895.

11 S. Ohta, S. Komagata, J. Seki, T. Saeki, S. Morishita and T. Asaoka, *J. Power Sources*, 2013, **238**, 53–56.

12 R. D. Shannon, B. E. Taylor, A. D. English and T. Berzins, *Electrochem. Acta*, 1977, **22**, 783.

13 T. Okumura, T. Takeuchi and H. Kobayashi, *Solid State Ionics*, 2016, **288**, 248–252.

14 T. Okumura, T. Takeuchi and H. Kobayashi, *J. Ceram. Soc. Jpn.*, 2017, **125**, 276–280.

15 M. Tatsumisago, R. Takano, K. Tadanaga and A. Hayashi, *J. Power Sources*, 2014, **270**, 603–607.

16 T. Okumura, S. Taminato, Y. Miyazaki, M. Kitamura, T. Saito, T. Takeuchi and H. Kobayashi, *ACS Appl. Energy Mater.*, 2020, **3**, 3220–3229.

17 B. Lopez-Bermudez, W. G. Zeier, S. Zhou, A. J. Lehner, J. Hu, D. O. Scanlon, B. J. Morgan and B. C. Melot, *J. Mater. Chem. A*, 2016, **4**, 6972–6979.

18 F. Izumi and K. Momma, *Solid State Phenom*, 2007, **130**, 15–20.

19 F. Izumi and T. Ikeda, *Mater. Sci. Forum*, 2000, **321–324**, 198.

20 H. Chen, L. L. Wong and S. Adams, *Acta Crystallogr., Sect. B: Struct. Sci., Cryst. Eng. Mater.*, 2019, **75**, 18–33.

21 H. Chen and S. Adams, *IUCrJ*, 2017, **4**, 614–625.

22 K. Momma and F. Izumi, *J. Appl. Crystallogr.*, 2011, **44**, 1272–1276.

23 R. D. Shannon, *Acta Crystallogr., Sect. A: Cryst. Phys., Diffr., Theor. Gen. Crystallogr.*, 1976, **32**, 751–767.

24 G. Caglioti, A. Paoletti and F. P. Ricci, *Nucl. Instrum.*, 1958, **3**, 223–228.

25 T. Okumura, Y. Yamaguchi, M. Shikano and H. Kobayashi, *J. Mater. Chem.*, 2012, **22**, 17340.

26 T. Okumura, S. Taminato, T. Takeuchi and H. Kobayashi, *ACS Appl. Energy Mater.*, 2018, **1**, 6303–6311.

27 T. Okumura, T. Takeuchi and H. Kobayashi, *ACS Appl. Energy Mater.*, 2021, **4**, 30–34.

28 A. D. Pelton, *Bull. Alloy Phase Diagrams*, 1986, **7**, 228–231.

29 P. Bach, M. Stratmann, I. Valencia-Jaime, A. H. Romero and F. U. Renner, *Electrochim. Acta*, 2015, **164**, 81–89.

30 A. D. Pelton, *Bull. Alloy Phase Diagrams*, 1986, **7**, 142–144.